

A Possible Distance Bias for Type Ia Supernovae with Different Ejecta Velocities

M. R. Siebert,¹★ R. J. Foley,¹ D. O. Jones,¹ K. W. Davis^{1,2}

¹*Department of Astronomy and Astrophysics, University of California, Santa Cruz, CA 95064*

²*Department of Astronomy and Astrophysics, University of California Los Angeles, Los Angeles, CA 90095*

Accepted XXX. Received YYY; in original form ZZZ

ABSTRACT

After correcting for their light-curve shape and color, Type Ia supernovae (SNe Ia) are precise cosmological distance indicators. However, there remains a non-zero intrinsic scatter in the differences between measured distance and that inferred from a cosmological model (i.e., Hubble residuals or HRs), indicating that SN Ia distances can potentially be further improved. We use the open-source relational database *kaepora* to generate composite spectra with desired average properties of phase, light-curve shape, and HR. At many phases, the composite spectra from two subsamples with positive and negative average HRs are significantly different. In particular, in all spectra from 9 days before to 15 days after peak brightness, we find that SNe with negative HRs have, on average, higher ejecta velocities (as seen in nearly every optical spectral feature) than SNe with positive HRs. At +4 days relative to *B*-band maximum, using a sample of 62 SNe Ia, we measure a 0.091 ± 0.035 mag (2.7σ) HR step between SNe with Si II $\lambda 6355$ line velocities ($v_{\text{Si II}}$) higher/lower than $-11,000$ km s⁻¹ (the median velocity). After light-curve shape and color correction, SNe with higher velocities tend to have underestimated distance moduli relative to a cosmological model. The intrinsic scatter in our sample reduces from 0.094 mag to 0.082 mag after making this correction. Using the Si II $\lambda 6355$ velocity evolution of 115 SNe Ia, we estimate that a velocity difference >500 km s⁻¹ exists at each epoch between the positive-HR and negative-HR samples with 99.4% confidence. Finally at epochs later than +37 days, we observe that negative-HR composite spectra tend to have weaker spectral features in comparison to positive-HR composite spectra.

Key words: supernovae: general

1 INTRODUCTION

Type Ia supernovae (SNe Ia) are important tools for understanding the acceleration of the expansion of the Universe caused by dark energy (Riess et al. 1998; Perlmutter et al. 1999). SN Ia light-curve shape and color correlate with luminosity and a time series of photometric measurements of SNe Ia allow us to measure precise distances to these phenomena (Pskovskii 1977; Phillips 1993; Riess et al. 1996). As cosmological surveys continue to reduce their calibration uncertainty, systematic uncertainties related to the explosion physics of SNe Ia must also decrease or they will limit our ability to constrain dark energy properties (Jones et al. 2018a).

While light-curve shape and color are adequate to reduce the scatter in SN Ia distances to $\sim 8\%$ (Scolnic et al.

2018; Jones et al. 2019), more parameters may be needed to further improve precision. Hubble residuals (HRs) are the differences between the measured distance moduli and distance moduli inferred from a cosmological model. After making corrections for light-curve shape and color, the HR scatter cannot be explained by photometric uncertainty alone, and this *intrinsic* scatter could be related to progenitor environmental properties or explosion physics (Conley et al. 2011; Scolnic et al. 2018). Several studies (e.g., Kelly et al. 2010; Lampeitl et al. 2010; Sullivan et al. 2010) have all found that the HR of a SN Ia is correlated with its host-galaxy mass. Other studies have found that host-galaxy metallicity also correlate with corrected SN Ia luminosity (D’Andrea et al. 2011; Childress et al. 2013a; Pan et al. 2014). These measurements should be a proxy for a physical property of the progenitor system. Current cosmological analyses treat the host-galaxy mass-HR relationship as a

★ E-mail: msiebert@ucsc.edu

step function, yet we do not fully understand its origin or functional form (Childress et al. 2013b).

Rigault et al. (2013) first studied how SN properties correlated with local host-galaxy properties and found evidence for a HR step with local host-galaxy star formation rate (SFR). Rigault et al. (2018) found reduced evidence for a local SFR step after using an updated version of the SALT2 SN Ia model (Guy et al. 2010; Betoule et al. 2014), but found strong evidence for a local *specific* SFR (sSFR) step, and Roman et al. (2018) found similar evidence for a local step by measuring host-galaxy $U - V$ colors. Jones et al. (2018a) investigated the stellar masses and $u - g$ colors within 1.5 kpc of SN Ia explosion sites, finding evidence for a local mass step, but they could not definitively say that local properties are better correlated with SN Ia HRs than global properties or random information. Rose et al. (2019) found a correlation between HR and global host-galaxy age, but did not see evidence for a stronger local effect.

The UV spectra of SNe Ia could be a more direct probe of progenitor metallicity (e.g., Höflich et al. 1998; Lentz et al. 2000; Foley et al. 2008b; Sauer et al. 2008; Walker et al. 2012). Foley & Kirshner (2013) found that two “twin” SNe Ia (SNe 2011by and 2011fe) have very similar light curves, colors, and spectra, but different UV continua. They attribute this difference to a difference in progenitor metallicity. Foley et al. (2019) then showed that these SNe have different intrinsic luminosities, indicating that progenitor metallicity could be related to intrinsic scatter. Similar results were found for a larger, but more diverse sample (Foley et al. 2016). Pan et al. (2019) looked at a larger sample of SN Ia UV spectra and found that SN Ia HRs are positively correlated with progenitor metallicity; however, Brown & Crumpler (2019) did not find evidence for this UV flux-metallicity correlation. Currently, spectral properties are infrequently used to calibrate SNe Ia.

Numerous studies have quantified the potential for spectroscopic measurements to improve HR intrinsic scatter. Bailey et al. (2009) found that measuring flux ratios in specific wavelength bins could improve upon using light-curve parameters alone. Blondin et al. (2011) confirmed this result and investigated the relationships of several other spectral properties with HR. They found marginal evidence that measuring line velocities or absorption strengths improves HR scatter. Silverman et al. (2012b) looked at an independent sample and found that velocity did not lead to significantly decreased HRs when applied in combination with SALT2 light-curve shape and color parameters. All of these studies found that flux ratios were the best spectral indicators for improving HR scatter. $\mathcal{R}(6520/4430)$, $\mathcal{R}^c(4610/4260)$, and $\mathcal{R}^c(3780/4580)$ (Bailey et al. 2009; Blondin et al. 2011; Silverman et al. 2012b, respectively) were found to reduce HR scatter at $>2\sigma$ levels. Additionally, Zheng et al. (2018) modeled the relationship between peak magnitude, rise time, and photospheric velocity. They show that this model can significantly reduce HR scatter if high-velocity (HV) SNe are removed from the sample.

SNe Ia have a large diversity of observed ejecta velocities (Branch 1987). Benetti et al. (2005) found that a sample of SNe Ia have a large range of Si II $\lambda 6355$ velocity gradients, where the amplitude of the gradient correlates with velocity at maximum light. Wang et al. (2009) classified “High-Velocity” and “Normal” SNe Ia as SNe Ia above and below a

velocity of $\sim 11,800 \text{ km s}^{-1}$ respectively. For typical SNe Ia, the velocities derived from Si II $\lambda 6355$ do not correlate with the decline-rate parameter $\Delta m_{15}(B)$ (Hatano et al. 2000). Some have suggested that “High-Velocity” SNe come from different progenitor channels than “Normal” SNe (e.g., Foley et al. 2012b; Maguire et al. 2013; Wang et al. 2013). Additionally, Foley & Kasen (2011) (hereafter FK11) found that HV SNe Ia have redder intrinsic $B - V$ colors than Normal SNe Ia. FK11 suggested that this effect could be reproduced with an asymmetric explosion viewed at different angles. Using a sample of 1630 optical spectra of 255 SNe, Foley et al. (2011) (hereafter FSK11) measured a correlation between maximum-light ejecta velocity and intrinsic $B - V$ color (the velocity-color relationship; VCR). This result was also verified for high-redshift SNe Ia (Foley 2012). If there are intrinsic differences between SNe Ia with varying velocities, we might expect that our cosmological distance corrections do not fully account for these effects.

In this work, we aim to investigate whether any optical spectral properties of SNe Ia correlate with HRs. This work makes use of *kaepora*, a public, open-source relational database of SN Ia spectra that was recently presented by Siebert et al. (2019) (hereafter S19). This tool provides a large sample of homogenized SN Ia spectra and their associated metadata. For this analysis, we have updated *kaepora* with new metadata from the output of SALT2 fits to SN light curves (Jones et al. 2018a). This new version of *kaepora* is available online¹. Also included is a set of tools that is useful for spectroscopic analysis. In this work we primarily use composite spectra to investigate SNe Ia with varying HRs and control for spectral variation with phase and light-curve shape. These composite spectra cover a large wavelength range, and can provide more information about potential spectral feature trends than individual measurements (like ejecta velocities or equivalent widths).

In Section 2, we describe the subsample of SNe in *kaepora* that have HR measurements which we then use for this study. In Section 3, we present our HR-binned composite spectra and measure trends of spectral features with HRs. In Section 4, we summarize these spectral trends and discuss how they might impact cosmology. We conclude in Section 5.

2 METHODS

2.1 Sample

Version 1.1 of *kaepora* contains 4975 spectra of 777 SNe Ia. The majority of these data are sourced from the Center for Astrophysics (CfA) Supernova Program (Blondin et al. 2012), the Berkeley SN Ia Program (BSNIP; Silverman et al. 2012a), and the Carnegie Supernova Project (CSP; Folatelli et al. 2013) accounting for 51.9%, 25.6%, and 12.4% of the total spectra, respectively. While the CfA sample contains many spectra per SN (typically 7), the BSNIP spectra cover a much larger wavelength range (typical ranges of $\sim 3500 - 7500 \text{ \AA}$ and $\sim 3200 - 10000 \text{ \AA}$, respectively). We also include data from Gomez et al. (1996); Riess et al. (1997); Leonard et al. (2005); Blondin et al. (2006); Matheson et al. (2008);

¹ <https://msiebert1.github.io/kaepora/>

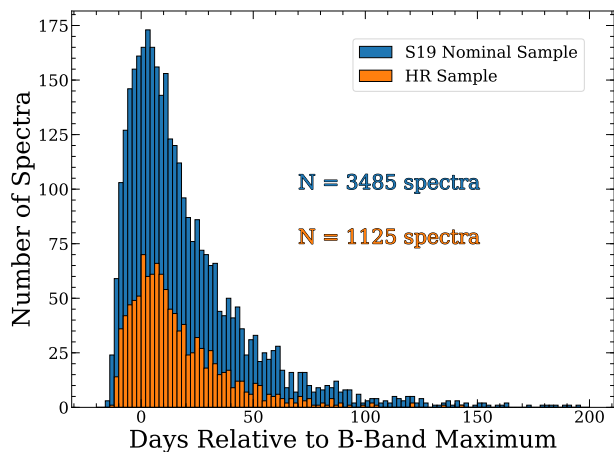


Figure 1. Blue and orange histograms of the number of individual spectra per SN in the S19 nominal and HR samples, respectively. The median phases are +12 and +10 days, respectively.

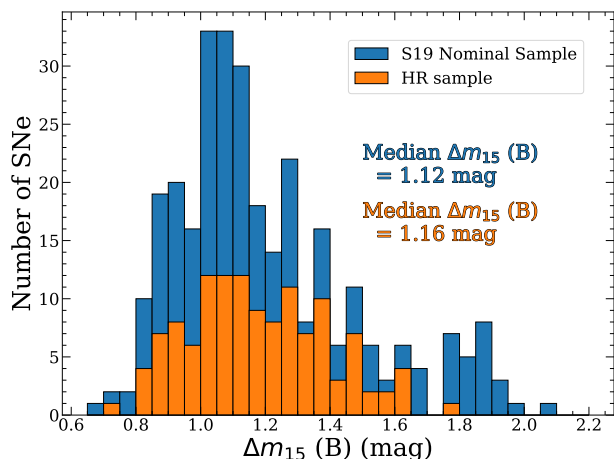


Figure 2. Blue and orange histograms of the number of SNe Ia per $\Delta m_{15}(B)$ bin in the S19 nominal and HR samples, respectively.

Foley et al. (2012b) and Silverman et al. (2015). This relational database allows for these data to be associated with a variety of useful SN-specific and spectrum-specific meta-data.

The spectral sample for this work is a subset of the “nominal” sample described in detail by S19. The nominal sample required SNe with a calibrated light curve that covered the time of maximum light and an MLCS2k2 (Jha et al. 2007) host-galaxy extinction estimate in order to correct the spectra for host-galaxy dust reddening. The MLCS2k2 light-curve fits adopt $R_V = 2.5$ since typical cosmological analyses often exclude highly reddened SNe Ia that seem to favor lower values of R_V (Kessler et al. 2009b; Burns et al. 2014). We also correct each spectrum for Milky Way (MW) reddening using the Schlafly & Finkbeiner (2011) reddening map, a Fitzpatrick (1999) reddening law, and $R_V = 3.1$.

2.2 Hubble Residual Measurements

The HRs used in this analysis are from Jones et al. (2018b), with the SN light curves themselves originating from CfA

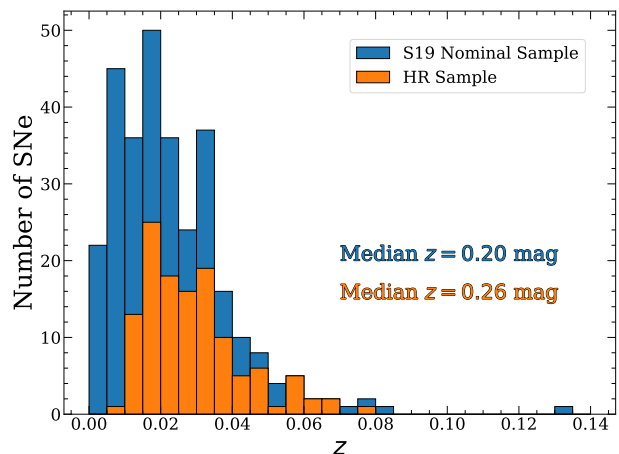


Figure 3. Same as Figure 2, but for redshift.

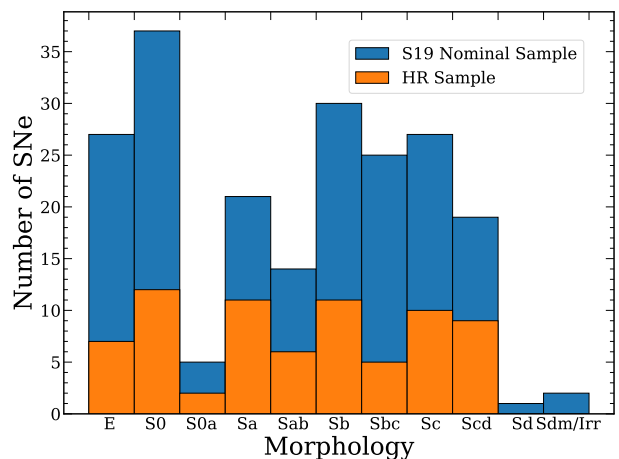


Figure 4. Same as Figure 2, but for host-galaxy morphology.

surveys 1-4 (Riess et al. 1999; Jha et al. 2006; Hicken et al. 2009, 2012) and CSP (Contreras et al. 2010; Folatelli et al. 2010; Stritzinger et al. 2011), with additional SNe from SDSS (Kessler et al. 2009b) and Pan-STARRS (Rest et al. 2014; Jones et al. 2018a; Scolnic et al. 2018) that are not included in this work. Notably, Foundation Supernova Survey light curves (Foley et al. 2018) are not included in this analysis, but will be in a future paper (Dettman et al., in prep.).

Light-curve fits to these data used the most recent version of the SALT2 model, SALT2.4 (Guy et al. 2010; Betoule et al. 2014). We also applied the selection criteria used in the Pantheon analysis (Scolnic et al. 2018) to ensure accurate distances. These include shape and color cuts that remove SNe with parameters outside the range for which the model is valid ($3 < x_1 < 3$, $0.3 < c < 0.3$) and cuts on the uncertainties of the shape and time of maximum light. We require MW reddening of $E(B - V) < 0.15$ mag and $z > 0.01$ to remove SNe that have distances with large peculiar-velocity uncertainties. The color cuts avoid SNe Ia with large dust reddening, which has been linked with atypical dust reddening and possible circumstellar scattering (e.g., Elias-Rosa et al. 2006; Wang et al. 2008; Phillips et al. 2013; Foley et al.

2014; Goobar et al. 2014) and has been linked to spectral differences (Wang et al. 2009; Mandel et al. 2014).

SN Ia distances are derived from the light-curve parameters using a version of the Tripp (1998) formula that includes the host-galaxy mass step, γ and a bias correction, $\Delta_B(z)$:

$$\mu = m_B - \mathcal{M} + \alpha \times x_1 - \beta \times c + \Delta_B(z) + \gamma. \quad (1)$$

Here, m_B is the light curve amplitude, \mathcal{M} is the SN absolute magnitude (whose exact value is degenerate with that of the Hubble constant and is irrelevant when only comparing HRs), and α and β are nuisance parameters that are determined from a fit to the full low- z sample. This fit is performed using the BEAMS with Bias Corrections (BBC) method of (Kessler & Scolnic 2017), which corrects for observational biases on the x_1 , c , and m_B parameters as well as on α and β . Those biases are estimated using large Monte Carlo simulations, generated with the SNANA software (Kessler et al. 2009a), to match the low- z samples observations and sample demographics. Biases are corrected with the $\Delta_B(z)$ term. We estimate HRs relative to the maximum likelihood distances in three redshift bins to remove any dependence on cosmological parameters.

2.3 Hubble Residual Spectroscopic Sample

This work investigates the intersection of the S19 nominal sample with the sample of SNe Ia for which we have also measured HRs (named the HR sample). These requirements limit the HR sample to 1125 spectra of 126 SNe Ia. The properties of this subsample are compared to those of the S19 nominal sample in Figures 1 – 4. Overall, the distributions of the parameters of the HR sample is similar to the S19 nominal sample. Since cosmological analyses cut out the fastest-declining SNe, the HR sample does not cover as wide a range of $\Delta m_{15}(B)$ as S19. The HR sample also has a slightly larger median redshift ($z = 0.026$ in the HR sample versus $z = 0.020$ in S19); this is because cosmological analyses only include SNe Ia in the Hubble flow where peculiar velocities of the SN host galaxies have a sufficiently small impact on distance measurements. It is also important to note that the HR sample only includes 7 spectra with $\tau > +100$ days compared to 131 spectra in the S19 nominal sample. Thus, analyses of the spectra in the HR sample at late phases are difficult to perform.

3 ANALYSIS

The general goal of this work is take an agnostic approach to investigating the spectral properties of SNe Ia that could be related to HRs determined with current photometric-only techniques. Several of the studies discussed in Section 1 first form a hypothesis about how certain observables (e.g., host SFR, progenitor metallicity, etc.) may correlate with HRs, then focus on those individual measurements. Here, we take an alternative approach where we assume that the intrinsic scatter is caused by physical differences that can manifest as spectral differences. This approach minimizes the bias associated with determining the importance of specific pre-determined observables, can more easily discover unexpected results, and if no differences are found, produces a

limit on the importance of spectral variability for reducing potential distance biases. *kaepora*, which both has tools to produce composite spectra for subsets of SNe and can easily control for properties known to correlate with the property in question (i.e., HR in this case), is uniquely designed for this kind of analysis. By looking at the average spectra of SNe with different HRs, we aim to determine which spectral properties (if any) correlate with HR.

3.1 Composite Spectra

In this work we generate Gini-weighted composite spectra using the methods presented by S19 for a variety of subsets of the HR sample. The Gini-weighting method provides a representative spectrum that maximizes the signal-to-noise ratio (S/N) while reducing the impact of individual high-S/N outliers. The basic algorithm is adapted from the methods used by Foley et al. (2008a) and Foley et al. (2012a). The composite spectra also contain information about the uncertainty and average properties (e.g., phase, $\Delta m_{15}(B)$, and redshift) as a function of wavelength. This information allows us to control for SN parameters that have known correlations with spectral features (such as phase and light-curve shape) as well as potentially unknown biases. S19 showed that a subset of spectra is well represented by a composite spectrum with the same average properties. We implement the same bootstrap resampling with replacement as in S19 in order to estimate the sample variation about the average spectrum.

In this work we use *kaepora* to provide subsets of SN Ia spectra that have similar average values of phase and $\Delta m_{15}(B)$ but different average HRs. By controlling for the main parameters that influence the diversity of SN Ia spectra, the remaining differences between composite spectra should be related to the parameter being varied. In this Section we present many of these Gini-weighted composite spectra. Due to the limitations of our sample size, we primarily present composite spectra generated using two HR bins (positive and negative). In Figure 5 we present five sets of maximum-light ($-2 < \tau < +2$ days) composite spectra constructed using these HR bins. From top to bottom, the composite spectra vary by the number of corrections that are made to the distance moduli of the contributing SNe.

First, we examine the composite spectra generated from SNe with positive and negative HRs when no light-curve shape, color, or mass-step corrections are applied. In this particular case, a SN with a negative HR has a higher peak luminosity and/or less host-galaxy dust extinction than a SN with a positive HR. The effective HR of these composite spectra are 0.22 and -0.24 mag, respectively. For these composite spectra, we see spectral differences between the positive-HR and negative-HR (higher peak luminosity) composite spectra that correspond to known trends in spectral features with light-curve shape. For example, the Si ratio ($\mathcal{R}(\text{Si II})$; Nugent et al. 1995) is smaller in the negative-HR composite spectrum. Additionally, the overall continuum of the negative-HR composite spectrum is bluer than the positive-HR composite spectrum, consistent with intrinsic colors of different luminosity SNe Ia. These results confirm that our method can reproduce expected spectral differences.

Applying only a color correction (i.e., correcting μ by

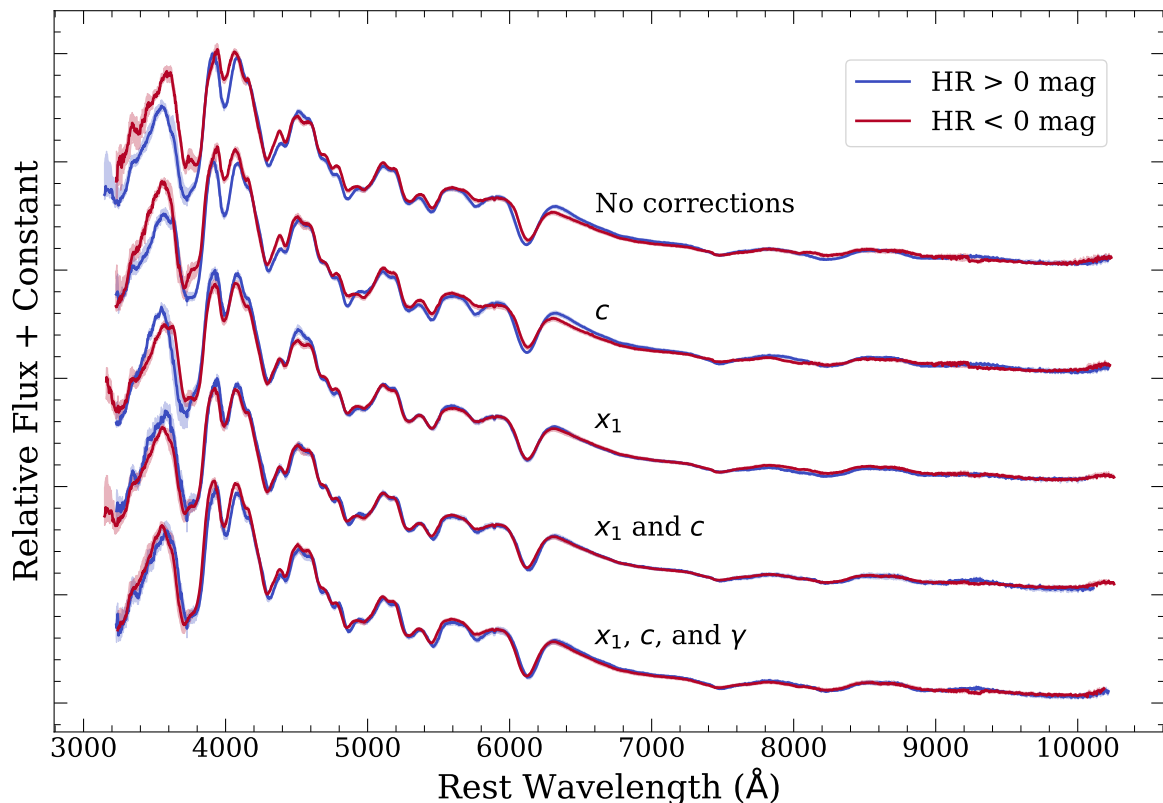


Figure 5. Four sets of maximum-light ($-2 < \tau < +2$ days) composite spectra constructed using positive- (blue) and negative-HR (red) bins. The shaded regions are the $1\text{-}\sigma$ bootstrap-sampling uncertainty for each composite spectrum. From top to bottom, the composite spectra vary in the distance modulus corrections that have been applied before measuring HRs. We start by using uncorrected luminosities, then subsequently correct for only light-curve shape (x_1); only color (c), light-curve shape and color (c); and light-curve shape, color, and host-galaxy mass step (γ). Most of the spectral variation between these two samples is removed after making the x_1 and c corrections.

$c\beta$) provides the biggest reduction in HR scatter for a single correction. The positive-HR and negative-HR composite spectra have effective HRs of 0.03 and -0.10 mag, respectively. Applying only a light-curve shape correction (i.e., correcting μ by αx_1) decreases the spectral differences of the positive-HR and negative-HR samples, but the HR difference does not decrease as significantly. The effective HR of the composite spectra for these subsamples are 0.24 and -0.22 mag, respectively. The spectral features of these composite spectra are well matched and the most notable difference is in the continua. The negative-HR composite spectrum (red curve labeled “ x_1 correction”) appears to be slightly redder in color than its positive-HR counterpart. Naively one might expect the opposite relationship (the distances of bluer SNe after light-curve shape correction should be underestimated if the difference corresponds only to a lack of a dust-reddening correction). However, if the x_1 correction also accounts for continuum differences in some way, then it is possible to have this relationship with a color correction necessary to match continua. There is also a slight difference in the Ca H&K and Ca NIR triplet features. The Ca features in the negative-HR composite spectrum are slightly weaker and at lower velocity than the positive-HR composite spectrum.

Correcting distance moduli for light-curve shape and color (correcting μ for both αx_1 and $c\beta$) yields HR-binned

composite spectra that are very similar. The continua are almost identical and the spectral feature strengths are well matched. The effective HR of these composite spectra are 0.10 and -0.12 mag, respectively, indicating that applying these distance modulus corrections has significantly reduced the HR scatter as expected.

Finally, introducing an additional host-mass step correction (γ) produces little change to the spectral features of the HR-binned composite spectra compared to those produced without making the host-mass correction. The effective HR of these composite spectra are 0.10 and -0.09 mag, respectively.

For the remainder of this work, composite spectra are generated using distance moduli that have been corrected for x_1 , c , and γ , corresponding to the values used in cosmological analyses, unless otherwise noted.

3.2 Hubble Residuals and Velocity

Despite having similar continua and overall line strengths, we observe a general trend that composite spectra generated from SNe with differing HRs tend to have different line velocities in many of their spectral features. In Figure 6, we present composite spectra generated from samples of SNe with positive and negative HRs (blue curve) and spectra with phases of $+2 < \tau < +7$ days. The positive-HR

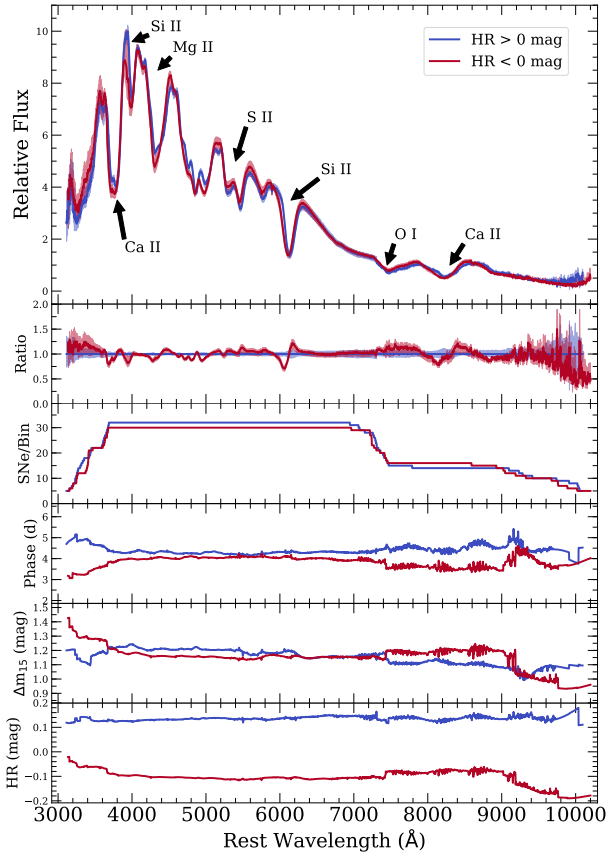


Figure 6. (First panel): +4-day composite spectra created from our nominal sample ($+2 < \tau < +7$ days, $0.7 \leq \Delta m_{15}(B) \leq 1.8$ mag). The blue curves show the properties of our positive-HR composite spectrum and the red curves show the properties of our negative-HR composite spectrum. The shaded regions are the $1\text{-}\sigma$ bootstrap sampling uncertainties. (Second panel): Ratio of the negative-HR composite spectrum relative to the positive-HR composite spectrum (red) and uncertainties on the positive-HR/negative-HR composite spectra (blue/red). (Third panel): Number of individual spectra contributing to each wavelength bin. (Fourth panel): Average phase relative to maximum brightness as a function of wavelength. (Fifth panel): Average value of $\Delta m_{15}(B)$ as a function of wavelength. (Sixth panel): The average HR as a function of wavelength.

and negative-HR composite spectra were constructed from 88 spectra of 30 SNe, and 65 spectra of 32 SNe, respectively. The composite spectra have effective phases of +4.4 and +3.8 days and effective values of $\Delta m_{15}(B)$ of 1.13 and 1.19 mag, respectively.

The positive-HR and negative-HR composite spectra have Si II $\lambda 6355$ line velocities of $-10,600 \text{ km s}^{-1}$ and $-11,580 \text{ km s}^{-1}$, respectively. Similar velocity shifts are also clearly visible for Ca H&K, Si II $\lambda 5972, 6355$, S II, and the Ca near-infrared (NIR) triplet (see the second panel of Figure 6). In regions where the continua are matched up well (e.g., Si II and the Ca NIR triplet), these differences are obvious in the ratio of the composite spectra.

Since the HR-binned composite spectra at +4 days show a dramatic difference in ejecta velocity, we also investigate the Si II line velocities of the individual SNe contributing to each composite spectrum. The +4-day composite spec-

tra contain data from 62 SNe whose velocity and HR measurements are shown in Figure 7 as black points (hereafter the “+4-day” HR sample). The orange stars are the velocity measurements made directly from the composite spectra displayed in Figure 6 and the shaded-blue violin regions depict the distributions of velocities measured from the individual output spectra from our bootstrap resampling process of each sample. At the top of Figure 7, we display HR histograms for the sample divided at $-11,000 \text{ km s}^{-1}$, the median velocity of the sample. We also display velocity histograms for positive-HR and negative-HR SNe on the right side of Figure 7.

There is no strong correlation between Si II velocity at +4 days and HR (absolute Pearson correlation coefficient of ~ 0.30), however there is some intriguing structure to the distribution of measurements. For example, there are no positive-HR SNe with velocities higher than $-12,000 \text{ km s}^{-1}$ in this phase bin. Using the uncertainties estimated from bootstrap resampling, we measure a velocity difference of $980 \pm 220 \text{ km s}^{-1}$ ($680 \pm 150 \text{ km s}^{-1}$ after removing $>2\sigma$ velocity outliers) between the positive-HR and negative-HR composite spectra. We perform a Kolmogorov-Smirnov test with high/low-velocity ($v_{\text{Si II}}$ below/above $-11,000 \text{ km s}^{-1}$) samples and find a p -value of 0.00031 (3.4σ), suggesting that we can reject the hypothesis that the HR distributions of these samples are drawn from the same population. We also perform a Kolmogorov-Smirnov test with positive-HR/negative-HR samples and find a p -value of 0.00078 (3.2σ), suggesting that we can also reject the hypothesis that the velocity distributions of these samples are drawn from the same population.

Despite the formally high significance of these tests, the HR uncertainties for individual objects are relatively large (typically 0.12 mag), and a large fraction of SNe have a sizeable probability of truly belonging to the opposite group than it is assigned. To include this uncertainty in our significance tests, we generate 10^6 realizations of the HR values in the +4-day sample, varying the HRs by a Gaussian distribution with a standard deviation corresponding to the uncertainty of the HR measurement. In Figure 8, we display HR as a function of Si II velocity at +4 days after maximum light. The black points and error bars are the same data as in Figure 7 (but the axes are swapped). The dark-blue curve is a two-parameter step function fit to the original data where the sample is split at the median velocity ($-11,000 \text{ km s}^{-1}$). The light-blue curves are 100 randomly chosen step-function fits to the resampled HR values. Using these data, we estimate a velocity step of $0.091 \pm 0.025 \text{ mag}$ (3.7σ). To investigate the importance of choosing the median velocity to separate the sample, we allowed the velocity that separates the samples to be a free parameter in our fit. Doing this, we measure a similar velocity step of $0.091 \pm 0.027 \text{ mag}$ (3.4σ), indicating that the exact choice of velocity to separate the sample is not driving the results. The removal of $>2\sigma$ velocity outliers also has a small impact on the step size ($0.087 \pm 0.025 \text{ mag}$). The low- and high-velocity samples have a sample intrinsic scatter of 0.108 mag and 0.064 mag, respectively. If we include the intrinsic scatter in the HR uncertainties, we measure a velocity step of $0.091 \pm 0.035 \text{ mag}$ (2.7σ).

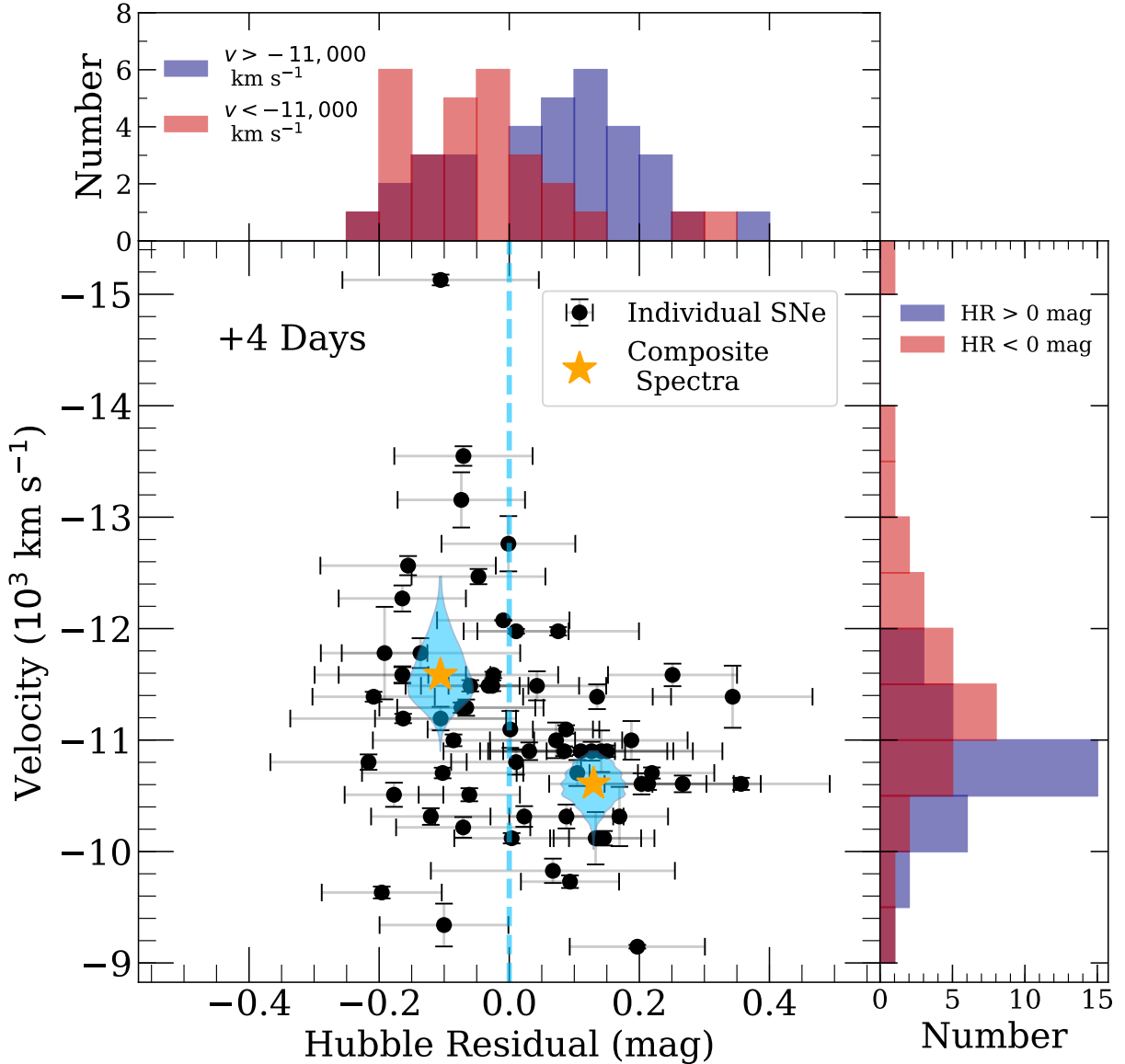


Figure 7. Si II velocity for individual SNe versus their HR (black points) for the sample of SNe contributing to our +4-day composite spectra in Figure 6. Orange stars correspond to the measurements from our composite spectra. The blue shaded region shows the distribution of velocities from bootstrap resampling. The vertical blue-dashed line at HR = 0 mag shows where the sample is divided. The top blue and red histograms display the distributions of HRs for SNe with $v > -11,000$ km s⁻¹ and $v < -11,000$ km s⁻¹, respectively. The right blue and red histograms display the distributions of velocities for positive-HR and negative-HR SNe, respectively.

3.3 Temporal Evolution of the Velocity-HR Trend

The velocity-HR trend is also visible over a large range of phases. In Figure 9 we present the Si II $\lambda 6355$ feature in six positive-HR (blue curves) and six negative-HR (red curves) composite spectra representing phases of approximately -9 ($\tau < -7$), -5 ($-7 < \tau < -2$), 0 ($-2 < \tau < +2$), $+4$ ($+2 < \tau < +7$), $+9$ ($+7 < \tau < +13$), and $+15$ ($+13 < \tau < +21$) days. At all epochs prior to +15 days after maximum light, we see that the Si II feature appears more blueshifted in the negative-HR composite spectra (red) than the positive-HR composite spectra (blue). These differences are apparent across a large range of velocities and often can not be accounted for by the 1σ bootstrapping uncertainty regions. The velocity difference manifests as a shift in the wavelength

of maximum absorption (from which we determine the velocity of the feature), the width of the feature, and the position of the blue edge of the feature. The full line profile provides additional information and evidence that the difference in ejecta velocity for the different HR subsamples is significant.

Using the relationships derived by Foley et al. (2011), we use the spectrum closest to maximum light to estimate $v_{\text{Si II}}^0$, the maximum-light Si II velocity, for each SN. With a sample of 115 SNe Ia we measure a $v_{\text{Si II}}^0$ -HR step of 0.068 ± 0.027 mag when the sample intrinsic scatter is included in the HR uncertainties. This is consistent with our step measurement from the +4-day sample (0.091 ± 0.035 mag).

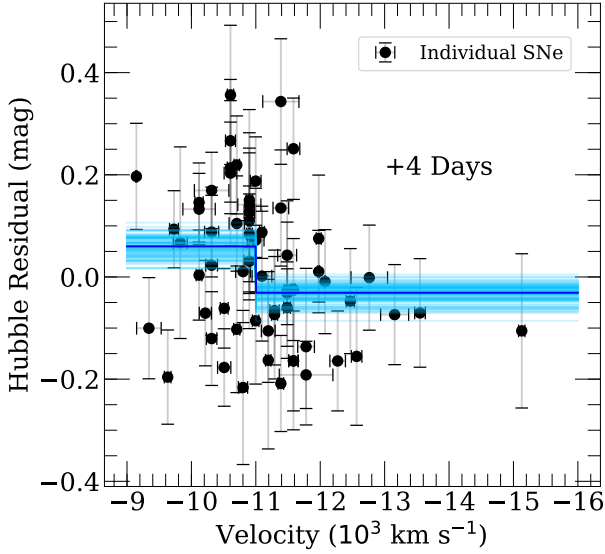


Figure 8. HR versus Si II velocity for individual SNe (black) in the +4-day sample. We fit a two-parameter step function (blue) to these data where we split the sample at the median velocity ($-11,000 \text{ km s}^{-1}$). The light-blue lines represent a subset of fits to random realizations of the data. The orange stars show measurements from composite spectra where we separate the sample at the same velocity. The best-fitting offset between two subsamples is $0.091 \pm 0.035 \text{ mag}$ offset (2.7σ).

3.4 Velocity-HR Trend Seen in Other Features

The velocity-HR trend is also visible in several absorption features besides Si II and over a large range of phases. Here we examine these other indicators of ejecta velocity correlating with HR.

In Figure 10 we display the spectral evolution of the Ca H&K, Si II $\lambda 4130$, Si II “W” feature, Si II $\lambda 5972$, $\lambda 6355$, and the Ca NIR Triplet in the same 6 sets of HR-binned composite spectra. We do not show composite spectra of the Ca NIR triplet at the earliest epoch because there are not enough SNe in the *kaepora* HR sample at that epoch to get 5 SNe per wavelength bin in that region. The fluxes of the HR-binned composite spectra have been rescaled in each absorption region to best compare the line profiles.

In the majority of the negative-HR composite spectra (red), the minima of these absorption features appear blueshifted relative to their positive-HR counterparts (blue). With the exception of Si II, which shows a large velocity difference at -9 days, the largest discrepancies in velocity occur either in the maximum-light or +4-day composite spectra for each absorption feature. All of the Si II features ($\lambda 4130$, $\lambda 5972$, and $\lambda 6355$) are more blueshifted in the negative-HR composite spectra at every epoch except +15 days where they have similar velocities. Ca H&K appears more blueshifted in the negative-HR composite spectra at every epoch. However, the Ca NIR triplet is more variable. The early-phase (-5 and 0 days) composite spectra of this feature are very similar, but the later-phase composite spectra show the same velocity trend as the other spectral absorption features.

We further examined color-corrected flux ratios other authors found to correlate with HRs. For the highest-

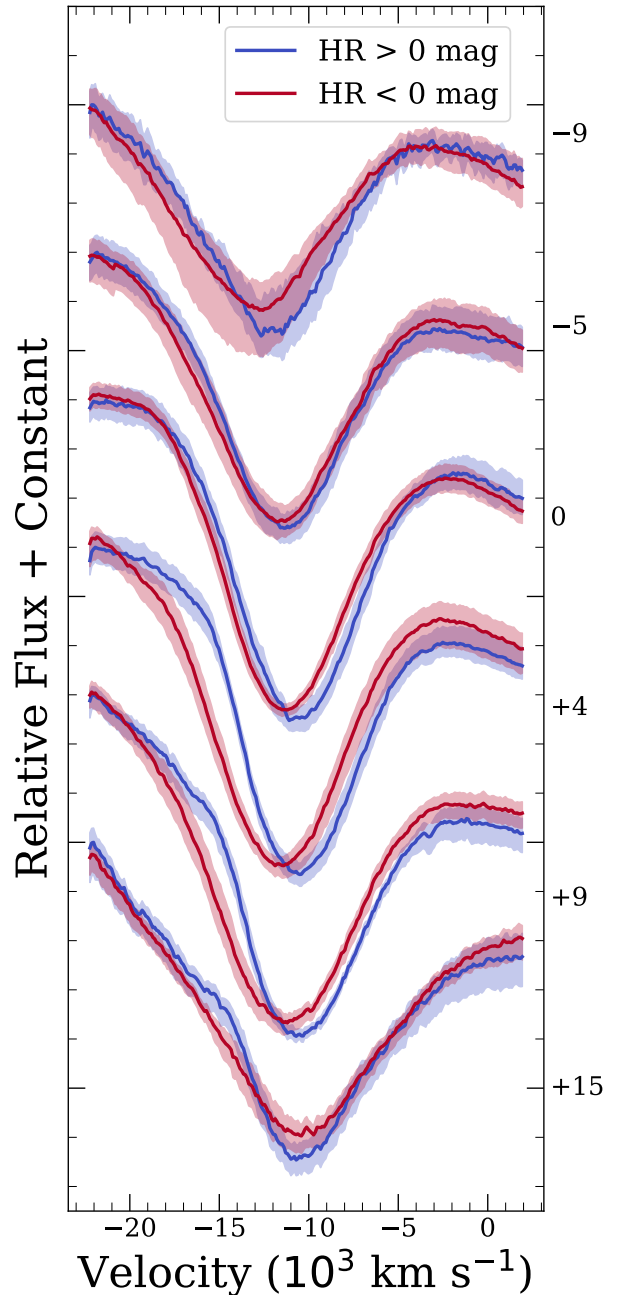


Figure 9. Time series of composite spectra created from subsamples of SNe with positive (blue) and (negative) HRs displaying the region around Si II $\lambda 6355$. The blue- and red-shaded regions are the $1\text{-}\sigma$ bootstrap-sampling uncertainties of the positive- and negative-HR composite spectra, respectively. The right vertical axis indicates the effective phase in days of each set of composite spectra. At all epochs prior to +15 days, the minimum of the main Si II feature is more blueshifted in the negative-HR sample than the positive-HR sample.

significance ratios, we find differences in the +4-day composite spectra. Notably, the two wavelengths used for a flux ratio (e.g., 4260 and 4610 \AA for $\mathcal{R}^c(4610/4260)$; Blondin et al. 2011) are at the edges of a spectral feature (in the example, Mg II). For these cases, the flux ratio changes significantly with velocity since the edge of a feature will shift, adjusting

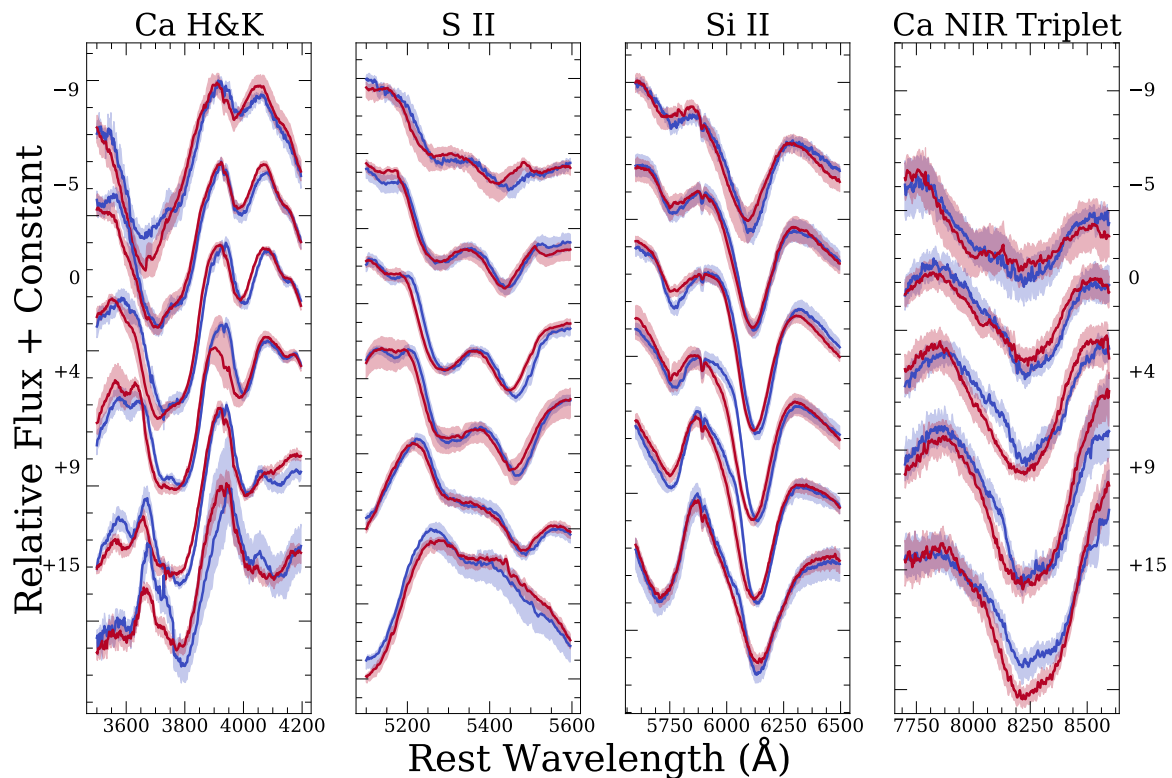


Figure 10. Time series of composite spectra created from subsamples of SNe with positive (blue) and (negative) HRs focusing on the Ca H&K (first panel), S II (second panel), Si II (third panel), and Ca II NIR triplet (fourth panel) features. Blue and red curves/shaded regions correspond to the positive-HR and negative-HR composite spectra respectively. The effective phase from top to bottom of the sets of composite spectra are -9 (excluding the Ca II NIR triplet), -5 , 0 , $+4$, $+9$, and $+15$ days.

the flux at a particular wavelength. We do not find evidence for different line strengths beyond the velocity difference for these measurements.

3.5 Hubble Residuals and Color Curves

Despite the velocity differences observed in the spectral absorption features, the continua are similar. We examine this in more detail by synthesizing $B - V$ and $V - i$ color curves, which we present in Figure 11.

The color curves of the HR-binned composite spectra look very similar. There is some tentative evidence that the positive-HR sample is redder than that of the negative-HR sample at $\tau \gtrsim 30$ days, while the $V - i$ color of positive-HR sample is bluer. This potential trend is discussed further in Section 4.

3.6 Hubble Residuals and Absorption Strength

In addition to the velocity-HR relationship discussed above, we also see an indication of spectral deviations between HR-binned samples at phases 1–3 months after peak. In Figure 12 we present three sets of HR-binned composite spectra with effective phases of $+37$, $+52$ and $+77$ days from top to bottom, respectively.

At $+37$ days, the positive-HR and negative-HR composite spectra look very similar. While there are some subtle differences, most of these deviations are contained within

the $1\text{-}\sigma$ bootstrap resampling uncertainty regions. However, as the composite spectra progress to later phases, the differences become more significant.

In the three displayed spectra, the negative-HR composite spectrum has weaker features than the positive-HR composite spectrum. This relationship is most obvious in the $+52$ -day HR-binned composite spectra, but is also significant in the $+77$ -day HR-binned composite spectra, but with a limited wavelength range and fewer SNe contributing. For this reason, we chose to further examine this trend by examining the $+52$ -day composite spectra in more detail.

Figure 13 is the same format as Figure 6 and shows these composite spectra along with some more detailed, wavelength-dependent information. These composite spectra were constructed using a phase bin of $+42 - +62$ days and $\Delta m_{15}(B)$ bins of $0.7 - 1.8$ mag. The effective phase, $\Delta m_{15}(B)$, and HR of the positive-HR composite spectrum are 50.8 days, 1.11 mag, and 0.09 mag, respectively (52.4 days, 1.08 mag, and -0.11 mag, for the negative-HR composite spectrum, respectively). While the phase bin is large, the average phase only differs by more than 3 days ($<5\%$ of the time since explosion) in 6% of all wavelength bins. Similarly for $\Delta m_{15}(B)$ (fifth panel), the average $\Delta m_{15}(B)$ at every wavelength only differs by more than 0.1 mag in 14% of wavelength bins. It is also noteworthy that the positive-HR and negative-HR sample sizes are very different in this phase range. With the positive-HR sample containing 18 spectra of 11 SNe, and the negative-HR sample containing 60 spec-

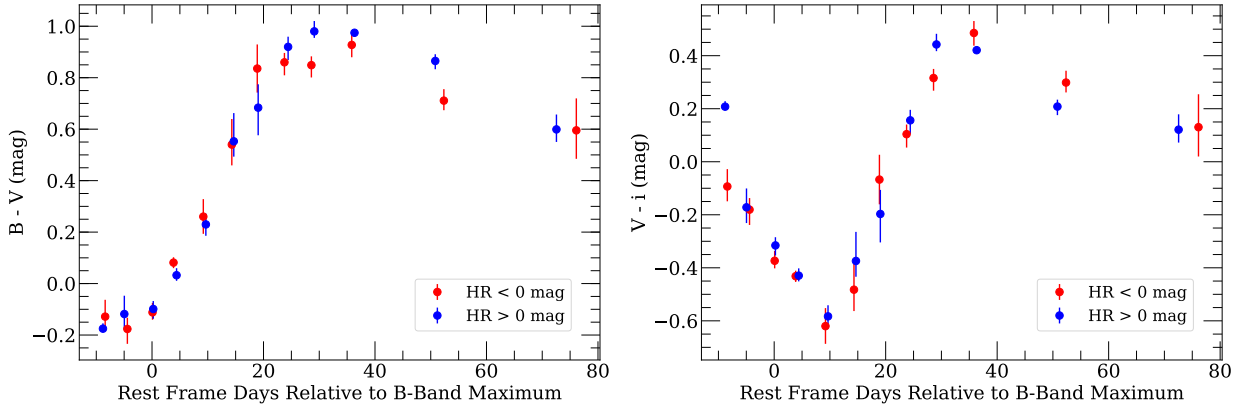


Figure 11. $B - V$ (left) and $V - i$ (right) color curves of our positive- (blue) and negative (red) composite spectra.

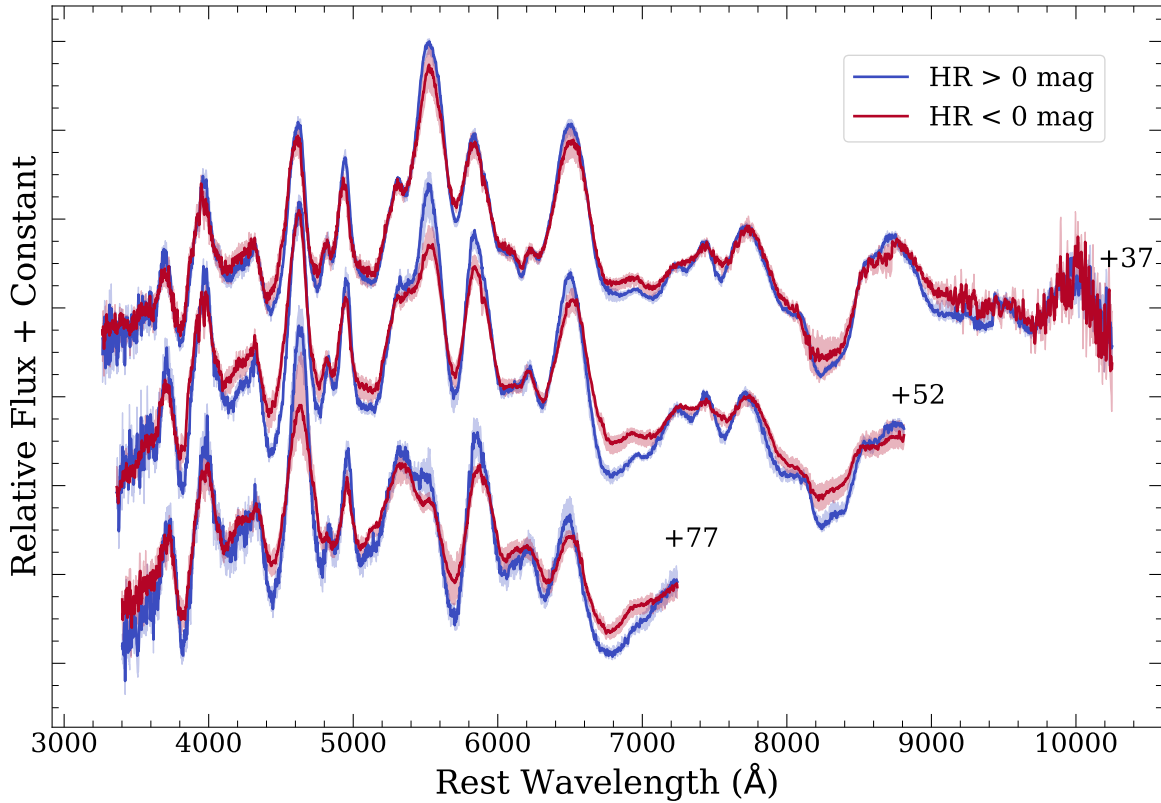


Figure 12. HR-binned composite spectra. Composite spectra with effective phases of +37, +52, and +77 days from top to bottom. Blue and red curves/shaded regions correspond to the positive- and negative-HR composite spectra, respectively.

tra of 31 SNe. While these spectral differences seen at these later epochs are intriguing, the small number of contributing SNe limits our inference.

A difference like this could be attributed to a difference in the overall continuum level of SNe with different HRs. The fractional depth of spectral features in SNe Ia with a larger overall flux levels should be smaller. Wang et al. (2019) has suggested that a B -band offset in HV SNe at phases $> +40$ days could be due to a light echo from circumstellar dust. A light echo could dilute the spectral features. However, our composite spectra do not exhibit a large color

difference at this phase (Section 3.5), disfavoring a light-echo explanation for the difference in spectral feature strength.

It is also possible that host-galaxy light contamination is causing the observed feature strength differences. This could also change the continuum level, diluting the strength of features. Since the difference between the spectra does not look like a galaxy spectrum, this scenario is less likely. Since there are only 11 SNe in the positive-HR sample, we caution interpretation of this difference until a larger sample is obtained.

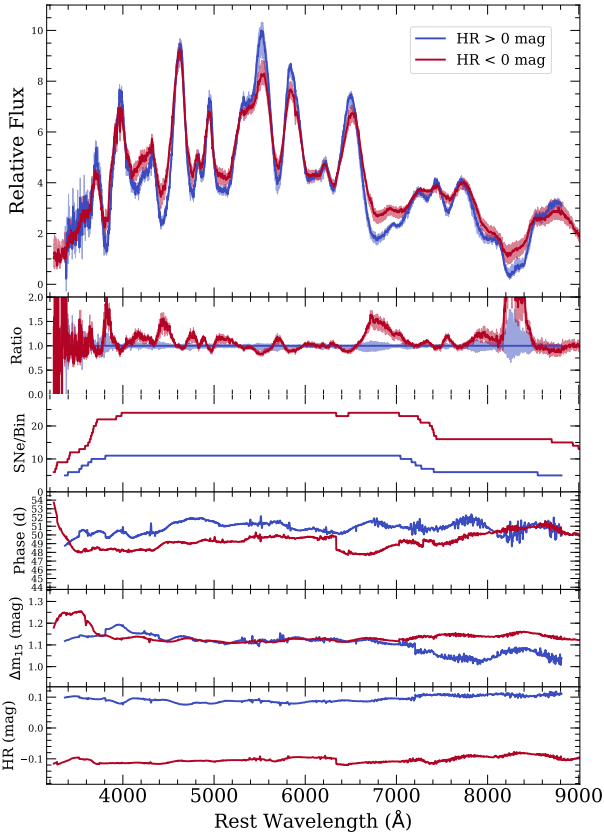


Figure 13. Same as Figure 6 but comparing the +52-day HR-binned composite spectra.

4 DISCUSSION

Composite spectra provide an agnostic approach to understanding spectral correlations with HR. Through this approach we find that velocity is the most important optical spectroscopic indicator of HR after all typical corrections are made. Quantifying the significance of the velocity-HR relationship is challenging since we observe this trend in several spectral absorption features and at several epochs. Most methods yield a statistically significant result.

We find that SNe with negative HRs tend to have higher ejecta velocity. Similarly, we find that SNe with higher ejecta velocity tend to have negative HRs after all light-curve and host-galaxy corrections are applied. That is, using modern techniques as done for cosmological analyses, SNe Ia with high (low) ejecta velocity have measured distance that are biased low (high).

In this section, we further discuss the significance of our results, and the implications a velocity distance bias would have on SN Ia cosmology results.

4.1 Temporal Velocity Evolution and HR Differences

In Figure 14, we further examine the evolution of $v_{\text{Si II}}$. The individual blue (red) points correspond to Si II $\lambda 6355$ velocity measurements from individual spectra whose SNe have positive-HR (negative-HR). The solid blue and red points connected by lines are the 2-day binned medians of

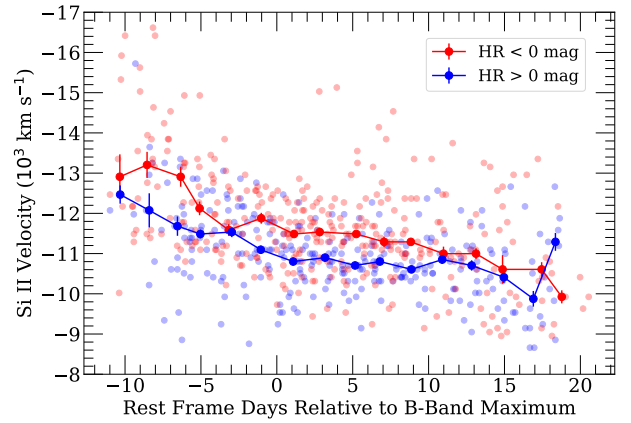


Figure 14. Si II velocity evolution for the HR sample. Individual points are measurements made from individual spectra. Solid connected points are binned medians using the bin sizes of 2 days and the error bars are the median absolute differences, dividing by the square-root of the number of points in a bin, for each bin. Blue and red points correspond to measurements from SNe in the positive-HR and negative-HR samples, respectively. We estimate that the negative-HR sample has a mean velocity that is at least 500 km s^{-1} larger than the positive-HR sample at the 2.8σ level.

these velocity measurements, and the error bars are the median absolute difference within each bin. While the scatter is large, it is clear that the negative-HR sample has consistently higher velocities on average than the positive-HR sample until $\sim +15$ days after maximum light. Over all bins in this phase range, the negative-HR sample is on average 500 km s^{-1} above the positive-HR sample, consistent with the +4-day subsample.

However, it is also important to note that these median measurements are correlated. While the phase bins do not overlap and individual measurements contribute to only a single median value, the same SN may have multiple spectra that cover a range of phases. We quantify this correlation with a simple Monte Carlo simulation. The positive-HR and negative-HR samples displayed in Figure 14 contain data from 52 and 62 SNe, respectively. From the full sample, we randomly generate two samples of SNe with these sample sizes. Each SN maintains all of its original velocity measurements. In our original measurements, the negative-HR sample has a higher median velocity in 14 out of 16 phase bins and has a median ejecta velocity higher by at least 500 km s^{-1} in 9 out of 16 phase bins. We find that the mock negative-HR sample produces a similar distribution of velocity residuals by chance in only 0.6% of trials.

4.2 Impact of SALT2 Corrections

We examine the impact of the velocity difference on distance modulus biases and cosmological analyses. In Figure 15 we present the maximum-light HR-binned composite spectra from Figure 5 focusing on the Si II $\lambda 6355$ feature. As in Figure 5, the top to bottom sets of positive-HR (blue) and negative-HR (red) composite spectra have increasing corrections applied before calculating HRs.

We find that for both the x_1 and c -corrected and x_1 , c , and γ -corrected composite spectra, the negative-HR com-

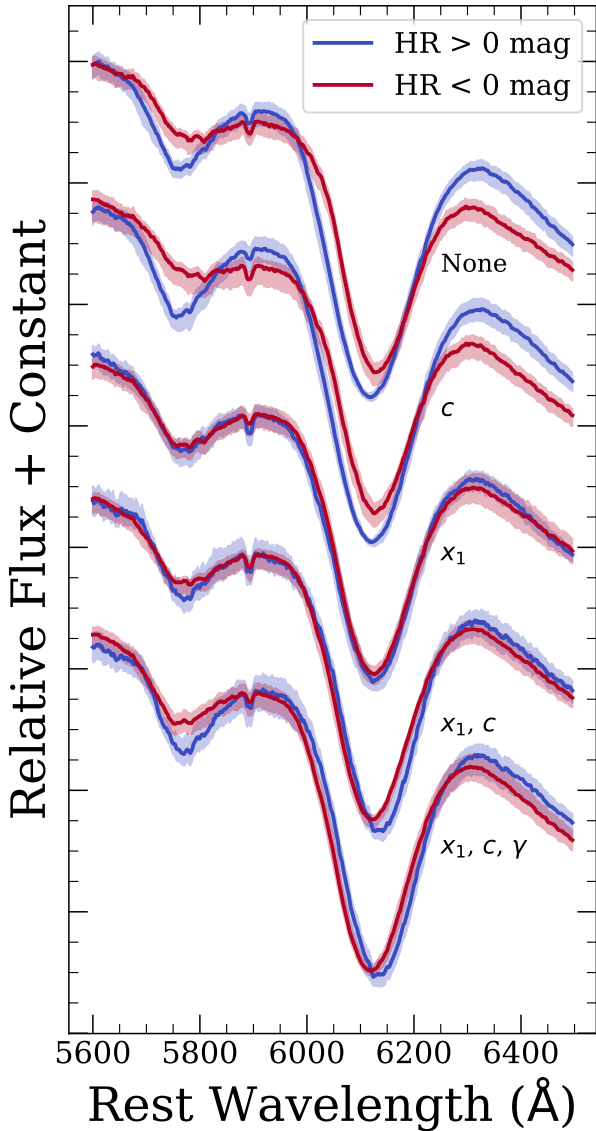


Figure 15. Same as Figure 5 but zoomed in on the Si II $\lambda 6355$ feature.

posite spectra clearly have a higher $v_{\text{Si II}}$ than positive-HR composite spectra. This means that the effect is present regardless of if a host-mass step (γ) correction is applied. Additionally, we are not introducing a velocity-HR correlation when accounting for the host-mass step. When we only apply the x_1 correction (third set of composite spectra), the velocity difference between the HR bins disappears indicating that, if there is still a velocity effect, it is not a dominant influence on HRs.

4.3 Consistency with Predictions from FSK11

The trend between HR and velocity has important implications for cosmological analyses. Here we quantify the improvement of precision obtained by applying the velocity step presented in Figure 8.

The intrinsic HR scatter for a sample is defined as the additional uncertainty required to achieve $\chi^2_{\nu} = 1$.

The intrinsic scatter in the +4-day sample improves from 0.094 mag to 0.082 mag after applying the velocity step. This improves the distance precision of each SN by 20%. However, this result is not significant (0.5σ). While potentially intriguing, this result is also still consistent with Blondin et al. (2011) and Silverman et al. (2012b), who found a $<10\%$ improvement in the HR weighted root-mean square (WRMS) when accounting for SN Ia maximum-light velocities. Despite the small improvement, Blondin et al. (2011) found evidence for a weak correlation between $v_{\text{Si II}}^0$ and x_1/c -corrected HRs (absolute Pearson correlation coefficient of 0.40).

FSK11 noted a correlation between velocity and color (VCR), which could have implications for a HR bias. FSK11 measured an intrinsic color by comparing the color of a SN to the expected color for a SN with a similar light-curve shape corrected peak brightness that is only reddened and dimmed by dust. Deviations in color from the expected relationship were interpreted as intrinsic.

FSK11 found a linear correlation between Si II velocity at maximum light and $(B_{\text{max}} - V_{\text{max}})_0$, the intrinsic difference between maximum B - and V -band brightnesses (the velocity-color relationship; VCR). Specifically, they found

$$(B_{\text{max}} - V_{\text{max}})_0 = (-0.39 \pm 0.04) - (0.033 \pm 0.004) \times \left(v_{\text{Si II}}^0 / 1000 \text{ km s}^{-1} \right). \quad (2)$$

Since the SALT2 c parameter behaves in a similar way to $B - V$ color Guy et al. (2005), the VCR should produce, assuming SALT2 does not somehow account for this affect already, a step between low- and high-velocity SNe of

$$\text{HR}_{\text{low}} - \text{HR}_{\text{high}} \approx (0.033 \pm 0.004) \times \frac{v_{\text{low}} - v_{\text{high}}}{1000 \text{ km s}^{-1}} \times \beta, \quad (3)$$

where $\beta = 3.15$ and “low” and “high” subscripts correspond to average measurements from the $v_{\text{Si II}} > -11,000 \text{ km s}^{-1}$ and $v_{\text{Si II}} < -11,000 \text{ km s}^{-1}$ subsamples, respectively.

The prediction that higher-velocity SNe should have negative HRs is a direct prediction from the direction of the correlation between velocity and color and is independent of our measurements. However, we now use mean velocity measurements of the low- and high-velocity +4-day HR samples ($-10,510$ and $-11,880 \text{ km s}^{-1}$, respectively) to estimate that VCR should produce a HR step of 0.14 ± 0.04 mag for our sample. This step size is consistent with the HR step that we observe (0.091 ± 0.025 mag) and has an important physical interpretation. Higher-velocity SNe Ia, which have redder intrinsic continua, are over-corrected for their color, making them appear closer away than they are. Notably, this would lead to corrected magnitudes that are brighter (negative-HR) than lower-velocity SNe Ia. Since the distribution of c values within our high- and low-velocity subsamples are very similar, we suggest that c does not fully account for intrinsic color differences due to velocity. The reduction in intrinsic scatter that we measure could indicate that chromatic scatter could account for $\sim 20\%$ of the observed intrinsic scatter.

While our measurement is consistent with the prediction of FSK11, there is significant overlap between the FSK11 sample and the HR sample presented in this work. Although FSK11 did not examine HRs, it should not be surprising that we observed a similar HR offset if that offset is caused by VCR.

Given the VCR presented in Foley et al. (2011), we

might expect the colors of our HR-binned composite spectra to be different. However, we do not see significant differences in the $B - V$ and $V - i$ colors curves presented in Figure 11. This may not be inconsistent since the continua are corrected using a reddening estimate from MLCS (Jha et al. 2007), while the HR is determined from SALT2 (Guy et al. 2010). It is possible that MLCS, which attempts to separate intrinsic color and dust reddening is less affected by the VCR.

FK11 found that when using the rudimentary corrections of $\Delta m_{15}(B)$ and peak color, accounting for the VCR improved the HR scatter from 0.190 to 0.130 mag. By using velocity, our results do not rule out an improvement of this size. Again, this consistency is not unexpected since the samples in FK11 and this work are not completely independent.

5 CONCLUSIONS

We have used the open-source relational database *kaepora* to generate a variety of composite spectra with different average properties in order to investigate potential spectral variation with HRs. Using sets of composite spectra, we further examine how SNe Ia with different HRs differ spectroscopically. Our main results can be summarized as follows:

(i) There are several spectral differences between SNe Ia with different HRs. This indicates both that current distance estimators that rely on photometric and host-galaxy measurements alone are not capturing the full physical diversity of SNe Ia and that measuring these spectral differences provides the possibility of improving distance measurements.

(ii) There exists a trend between Si II velocity and HR. Using a sample of 62 SNe Ia, we find that SNe with negative-HRs tend to have higher Si II $\lambda 6355$ velocities. We measure a HR-Si II $\lambda 6355$ velocity step at $-11,000 \text{ km s}^{-1}$ of $0.091 \pm 0.035 \text{ mag}$. This step is consistent with a VCR (Foley et al. 2011), and correcting for the velocity step may improve distance precision by 20%.

(iii) Using all individual spectra ranging from -13 to $+22$ days, we find 2.8σ evidence for a Si II $\lambda 6355$ velocity difference $>500 \text{ km s}^{-1}$ between the positive-HR and negative-HR samples at all epochs.

(iv) A similar velocity offset between positive-HR and negative-HR samples is observed at a variety of epochs and in multiple spectral features. For negative-HR composite spectra we observe larger blueshifts in Ca H&K, Si II $\lambda 4130$, Si II $\lambda 5972$ and $\lambda 6355$, and the Ca II NIR triplet, and at phases of -9 to $+15$ days. The differences are apparent across the line feature, with the negative-HR spectra having broader features with bluer blue edges. In many different ways across phase, atomic species, and line profile, the negative-HR SNe have indications of higher ejecta velocity, making the above results more significant. Additionally, we use near-maximum light spectra to estimate $v_{\text{Si II}}^0$ for a sample of 115 SNe Ia. With these measurements we estimate a $v_{\text{Si II}}^0$ -HR step of $0.068 \pm 0.027 \text{ mag}$ when sample intrinsic scatter is included in HR uncertainties.

(v) Using our maximum-light composite spectra, we find that this velocity difference is apparent for HRs derived with and without accounting for the host-galaxy mass step. This

indicates that the velocity difference is not induced by making this distance modulus correction, and the host-mass step is not caused by velocity.

(vi) At late epochs ($+37 - 77$ days) we observe that the negative-HR sample produce composite spectra that appear to have overall weaker spectral features than the positive-HR sample. This difference appears to strengthen with time, however, more spectra are needed to validate this effect.

(vii) All results are consistent with a VCR (FSK11). In this scenario, high-velocity SNe Ia have intrinsically redder continua than low-velocity SNe. The redder continua is over-corrected using current distance estimators, causing a distance bias.

A velocity-HR step of $\sim 0.1 \text{ mag}$ has important implications for cosmological analyses. Currently there is not significant evidence that the velocity distributions of SNe Ia evolve with redshift (Blondin et al. 2006; Foley 2012). However if the average velocity changes with redshift, we would introduce a systematic bias in our cosmological parameter estimates. We should gather more high-redshift spectra to further explore this effect. Specifically, we have presented evidence that the velocity-HR trend manifests as a velocity difference in numerous absorption features. These potential differences should be further explored in both low- and high-redshift samples. Also, Léget et al. (2019) recently developed SUGAR to improve the spectral description of SNe Ia. Using a “PCA-like” method, they showed that the second-most important factor was strongly correlated with Si II and S II velocity. The variation in this factor was also related to variation in color, and was not correlated with the SALT2 x_1 or c parameters. This supports our conclusion that SALT2 does not fully capture spectral variations associated with ejecta velocity.

Since ejecta velocity trends with HR, we encourage more spectral observations of SNe Ia, perhaps especially immediately after maximum light ($+2 - +7$ days) to provide the best unbiased distance measurements and to increase sample sizes. Since the VCR is consistent with our observations, it might be possible to glean additional distance information from color curves without directly measuring velocities. However with our current sample and techniques, we do not see significant differences in the $B - V$ or $V - i$ color curves of our HR-binned composite spectra at a variety of epochs. This indicates that spectra are likely needed to fully capture the velocity effect. While the spectral differences at later phases should be further explored, it is less feasible to get spectroscopic follow-up observations of SNe Ia in a cosmological sample at these late epochs.

Future cosmological experiments such as the Large Synoptic Survey Telescope (LSST) and the *Wide-Field InfraRed Space Telescope* (WFIRST) will discover and photometrically follow large samples of SNe Ia ($10^5 - 10^6$), but only a small fraction will have spectroscopy (Hounsell et al. 2018; The LSST Dark Energy Science Collaboration et al. 2018). Careful choices must be made, especially now that WFIRST’s spectroscopic capabilities are limited to a slitless prism and grisms, to fully sample the velocity distribution and to determine if that distribution changes with redshift. The velocity-HR effect must be analyzed in detail to properly plan for and leverage these experiments.

ACKNOWLEDGEMENTS

M.R.S. is supported by the National Science Foundation Graduate Research Fellowship Program Under Grant No. 1842400. D.O.J. is supported by a Gordon & Betty Moore Foundation postdoctoral fellowship at the University of California, Santa Cruz. The UCSC team is supported in part by NASA grant NNG17PX03C; NSF grants AST-1518052 and AST-1815935; the Gordon & Betty Moore Foundation; the Heising-Simons Foundation; and by a fellowship from the David and Lucile Packard Foundation to R.J.F.

REFERENCES

- Bailey S., et al., 2009, *A&A*, **500**, L17
- Benetti S., et al., 2005, *ApJ*, **623**, 1011
- Betoule M., et al., 2014, *A&A*, **568**, A22
- Blondin S., et al., 2006, *AJ*, **131**, 1648
- Blondin S., Mandel K. S., Kirshner R. P., 2011, *A&A*, **526**, A81
- Blondin S., et al., 2012, *AJ*, **143**, 126
- Branch D., 1987, *ApJ*, **316**, L81
- Brown P. J., Crumpler N. R., 2019, arXiv e-prints, p. [arXiv:1909.05445](https://arxiv.org/abs/1909.05445)
- Burns C. R., et al., 2014, *ApJ*, **789**, 32
- Childress M. J., et al., 2013a, *ApJ*, **770**, 29
- Childress M., et al., 2013b, *ApJ*, **770**, 108
- Conley A., et al., 2011, *ApJS*, **192**, 1
- Contreras C., et al., 2010, *AJ*, **139**, 519
- D’Andrea C. B., et al., 2011, *ApJ*, **743**, 172
- Elias-Rosa N., et al., 2006, *MNRAS*, **369**, 1880
- Fitzpatrick E. L., 1999, *PASP*, **111**, 63
- Folatelli G., et al., 2010, *AJ*, **139**, 120
- Folatelli G., et al., 2013, *ApJ*, **773**, 53
- Foley R. J., 2012, *ApJ*, **748**, 127
- Foley R. J., Kasen D., 2011, *ApJ*, **729**, 55
- Foley R. J., Kirshner R. P., 2013, *ApJ*, **769**, L1
- Foley R. J., et al., 2008a, *ApJ*, **684**, 68
- Foley R. J., Filippenko A. V., Jha S. W., 2008b, *ApJ*, **686**, 117
- Foley R. J., Sanders N. E., Kirshner R. P., 2011, *ApJ*, **742**, 89
- Foley R. J., et al., 2012a, *AJ*, **143**, 113
- Foley R. J., et al., 2012b, *ApJ*, **752**, 101
- Foley R. J., et al., 2014, *MNRAS*, **443**, 2887
- Foley R. J., et al., 2016, *MNRAS*, **461**, 1308
- Foley R. J., et al., 2018, *MNRAS*, **475**, 193
- Foley R. J., Hoffmann S. L., Macri L. M., Riess A. G., Brown P. J., Filippenko A. V., Graham M. L., Milne P. A., 2019, *MNRAS*, p. 2970
- Gomez G., Lopez R., Sanchez F., 1996, *AJ*, **112**, 2094
- Goobar A., et al., 2014, *ApJ*, **784**, L12
- Guy J., Astier P., Nobili S., Regnault N., Pain R., 2005, *A&A*, **443**, 781
- Guy J., et al., 2010, *A&A*, **523**, A7
- Hatano K., Branch D., Lentz E. J., Baron E., Filippenko A. V., Garnavich P. M., 2000, *ApJ*, **543**, L49
- Hicken M., Wood-Vasey W. M., Blondin S., Challis P., Jha S., Kelly P. L., Rest A., Kirshner R. P., 2009, *ApJ*, **700**, 1097
- Hicken M., et al., 2012, *ApJS*, **200**, 12
- Höflich P., Wheeler J. C., Thielemann F.-K., 1998, *ApJ*, **495**, 617
- Hounsell R., et al., 2018, *ApJ*, **867**, 23
- Jha S., et al., 2006, *AJ*, **131**, 527
- Jha S., Riess A. G., Kirshner R. P., 2007, *ApJ*, **659**, 122
- Jones D. O., et al., 2018a, *ApJ*, **857**, 51
- Jones D. O., et al., 2018b, *ApJ*, **867**, 108
- Jones D. O., et al., 2019, *ApJ*, **881**, 19
- Kelly P. L., Hicken M., Burke D. L., Mandel K. S., Kirshner R. P., 2010, *ApJ*, **715**, 743
- Kessler R., Scolnic D., 2017, *ApJ*, **836**, 56
- Kessler R., et al., 2009a, *PASP*, **121**, 1028
- Kessler R., et al., 2009b, *ApJS*, **185**, 32
- Lampeitl H., et al., 2010, *ApJ*, **722**, 566
- Léget P. F., et al., 2019, arXiv e-prints, p. [arXiv:1909.11239](https://arxiv.org/abs/1909.11239)
- Lentz E. J., Baron E., Branch D., Hauschildt P. H., Nugent P. E., 2000, *ApJ*, **530**, 966
- Leonard D. C., Li W., Filippenko A. V., Foley R. J., Chornock R., 2005, *ApJ*, **632**, 450
- Maguire K., et al., 2013, *MNRAS*, **436**, 222
- Mandel K. S., Foley R. J., Kirshner R. P., 2014, *ApJ*, **797**, 75
- Matheson T., et al., 2008, *AJ*, **135**, 1598
- Nugent P., Phillips M., Baron E., Branch D., Hauschildt P., 1995, *ApJ*, **455**, L147
- Pan Y. C., et al., 2014, *MNRAS*, **438**, 1391
- Pan Y. C., Foley R. J., Jones D. O., Filippenko A. V., Kuin N. P. M., 2019, arXiv e-prints, p. [arXiv:1906.09554](https://arxiv.org/abs/1906.09554)
- Perlmutter S., et al., 1999, *ApJ*, **517**, 565
- Phillips M. M., 1993, *ApJ*, **413**, L105
- Phillips M. M., et al., 2013, *ApJ*, **779**, 38
- Pskovskii I. P., 1977, *Soviet Ast.*, **21**, 675
- Rest A., et al., 2014, *ApJ*, **795**, 44
- Riess A. G., Press W. H., Kirshner R. P., 1996, *ApJ*, **473**, 88
- Riess A. G., et al., 1997, *AJ*, **114**, 722
- Riess A. G., et al., 1998, *AJ*, **116**, 1009
- Riess A. G., et al., 1999, *AJ*, **117**, 707
- Rigault M., et al., 2013, *A&A*, **560**, A66
- Rigault M., et al., 2018, arXiv e-prints, p. [arXiv:1806.03849](https://arxiv.org/abs/1806.03849)
- Roman M., et al., 2018, *A&A*, **615**, A68
- Rose B. M., Garnavich P. M., Berg M. A., 2019, *ApJ*, **874**, 32
- Sauer D. N., et al., 2008, *MNRAS*, **391**, 1605
- Schlafly E. F., Finkbeiner D. P., 2011, *ApJ*, **737**, 103
- Scolnic D. M., et al., 2018, *ApJ*, **859**, 101
- Siebert M. R., et al., 2019, *MNRAS*, **486**, 5785
- Silverman J. M., et al., 2012a, *MNRAS*, **425**, 1789
- Silverman J. M., Ganesalingam M., Li W., Filippenko A. V., 2012b, *MNRAS*, **425**, 1889
- Silverman J. M., Vinkó J., Marion G. H., Wheeler J. C., Barna B., Szalai T., Mulligan B. W., Filippenko A. V., 2015, *MNRAS*, **451**, 1973
- Stritzinger M. D., et al., 2011, *AJ*, **142**, 156
- Sullivan M., et al., 2010, *MNRAS*, **406**, 782
- The LSST Dark Energy Science Collaboration et al., 2018, arXiv e-prints, p. [arXiv:1809.01669](https://arxiv.org/abs/1809.01669)
- Tripp R., 1998, *A&A*, **331**, 815
- Walker E. S., Hachinger S., Mazzali P. A., Ellis R. S., Sullivan M., Gal Yam A., Howell D. A., 2012, *MNRAS*, **427**, 103
- Wang X., et al., 2008, *ApJ*, **675**, 626
- Wang X., et al., 2009, *ApJ*, **699**, L139
- Wang X., Wang L., Filippenko A. V., Zhang T., Zhao X., 2013, *Science*, **340**, 170
- Wang X., Chen J., Wang L., Hu M., Xi G., Yang Y., Zhao X., Li W., 2019, *ApJ*, **882**, 120
- Zheng W., Kelly P. L., Filippenko A. V., 2018, *ApJ*, **858**, 104

This paper has been typeset from a \LaTeX file prepared by the author.